

Three-dimensional nature of ion transport in thin-layer electrodeposition

G. Marshall,^{1,3} E. Mocskos,¹ F. V. Molina,^{2,3} and S. Dengra¹

¹Laboratorio de Sistemas Complejos, FCEN, Universidad de Buenos Aires, 1428 Buenos Aires, Argentina

²INQUIMAE, FCEN, Universidad de Buenos Aires, 1428 Buenos Aires, Argentina

³Consejo Nacional de Investigaciones Científicas y Técnicas, 1428 Buenos Aires, Argentina

(Received 23 October 2002; published 18 August 2003)

A generalized three-dimensional model for ion transport in electrodeposition is introduced. Ion transport is mainly governed by diffusion, migration, and convection. When convection prevails, in particular, in the limiting case of gravity-driven convection, the model predicts concentration shells and convection rolls and their interaction mode with a deposit tip: shell and roll bend and surround the tip forming a three-dimensional envelope tube squeezed at the deposit tip. In the limiting case of electrically driven convection, a vortex ring and an electric spherical drop crowning the deposit tip are predicted. When gravity and electric convection are both relevant, the interaction of ramified deposits, vortex tubes and rings, and electric spherical drops, leading to complex helicoidal flow, is predicted. Many of these predictions are experimentally observed, suggesting that ion transport underlying dendrite growth is remarkably well captured by our model.

DOI: 10.1103/PhysRevE.68.021607

PACS number(s): 82.45.Qr, 47.20.Bp, 89.90.+n

I. INTRODUCTION

In a thin-layer electrochemical deposition (ECD) experiment, the electrolytic cell consists of two glass plates sandwiching two parallel electrodes and a metal salt electrolyte. A voltage difference applied between electrodes produces a treelike deposit by a reduction of the metal ions. The morphology of the deposit can be fractal, densely branched, or dendritic depending on the cell geometry, electrolyte concentration, cell voltage, and other parameters. The ECD phenomenon is a paradigmatic model for studying growth pattern formation [1–21]. Issues of ECD are particularly pertinent in the cases of bipolar electrodeposition [22,23] in the field of macrowiring, in which an applied electric field can be exploited to create directional growth of copper deposits between copper particles that are not connected to an external circuit, and in microwiring, in the assembly of a new class of microwires by dielectrophoresis from suspension of metallic nanoparticles [24]. In both techniques a complex flow near the tips of the growing wire was observed.

Beyond the dendrite growth complex physicochemical hydrodynamical ion transport processes take place. Ion transport is mainly governed by diffusion, migration, and convection. Convection is mostly driven by Coulombic forces due to local electric charges and by buoyancy forces due to concentration gradients that lead to density gradients. The relevance of convection, relative to migration and diffusion, for cells with thickness larger than $50\ \mu\text{m}$ has been demonstrated by a number of researchers [3–13]. In cells with thickness less than $50\ \mu\text{m}$, diffusion and migration are the dominant modes in ion transport [14].

Figures 1 and 2 show two snapshots of a narrow section of the cell with schlieren images of dendrites (darker pixels in Fig. 2) growing from the cathode (left) towards the anode. These experimental figures have been obtained in a similar way as those presented in Ref. [19]. The growth starts as a small roughness at the cathode and soon develops into full mature dendrites, already competing among themselves (Fig.

2). The struggle for survival is hard and few make contact with the anode, upon which they become a dead forest. During growth dendrites encounter incoming anodic fronts (bright pixels), whose nature is later explained, which suddenly change their growth speed and form.

When convection prevails in ion transport, the study of the relative weight of electroconvection *vis-à-vis* gravitoconvection is relevant because it determines the flow regime and thus ion transport and growth morphology. Several ways have been devised to analyze experimentally the above-mentioned problem through variations in cell thickness [12], carrying experiments with the cell in vertical position [12] or under microgravity conditions [25], and through electrolyte viscosity variations [21]. This problem is addressed here theoretically, through dimensional analysis, and with computer simulations.

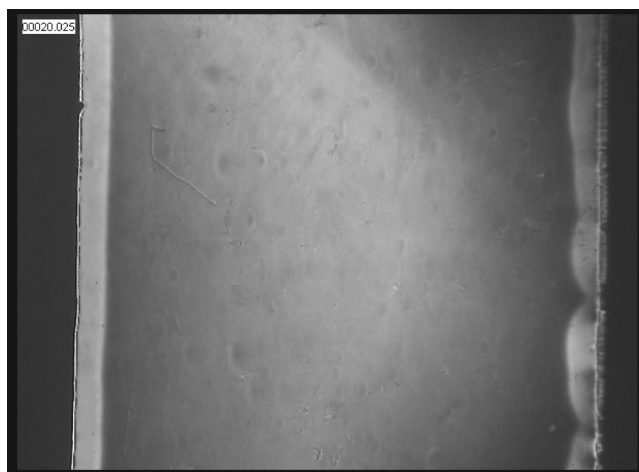


FIG. 1. Schlieren images of a narrow section of an electrolytic cell showing the first instants (20 s) after the circuit is closed: cathode and anode (dark pixels) and rolls (bright pixels), under a gravitoconvection prevailing regime. The copper sulfate solution concentration is $C=1.0\ \text{mol/l}$, the cell dimensions are $12\times 20\times 0.1\ \text{mm}^3$ and the applied voltage is 10 V.

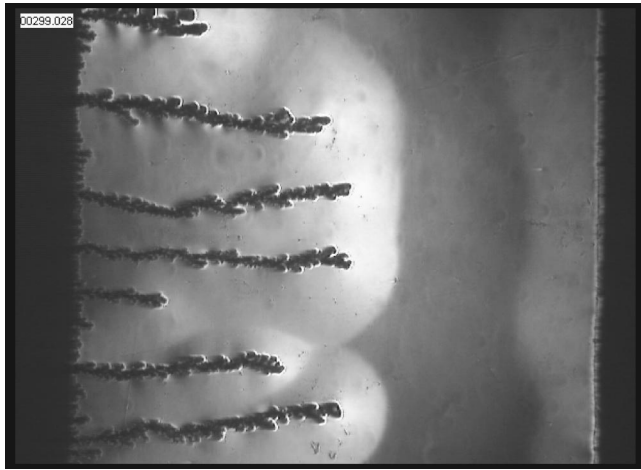


FIG. 2. Schlieren images of a partially developed dendrite growth (300 s).

Figure 3 shows a typical cell (in an horizontal position) used in ECD experiments. Here, the horizontal plane or x - y plane contains the electrodes and the growing dendrites (the cathode-anode distance, width, and depth of the cell are measured along the y , x , and z coordinates, respectively). For ease of interpretation, we refer as *top view*, to a cross section of the three-dimensional(3D) cell at constant z , as *side view*, to a cross section at a constant x , and as *front view* and *rear view*, to cross sections at a constant y (facing the cathode and anode, respectively). These conventions are illustrated in the figure.

Physically, in an ECD experiment, when the circuit is closed, current starts flowing through the cell and ion concentration boundary layers develop near each electrode. At the anode the concentration is increased above its initial level due to the transport of anions towards, and the dissolution of metal ions from the anode. At the cathode, the ion concentration is decreased as metal ions are reduced and deposited out and anions drift away. These concentration variations lead to density variations, and therefore to the development of gravity-driven convection rolls at the electrodes [12]. This is illustrated in Fig. 1, showing schlieren images of the cathodic and anodic concentration rolls (bright pixels) near the cathode and anode (dark pixels), respectively, and in Fig. 4 (reproduced from Ref. [12]) showing a side view of the cell, with a roll formed near the cathode. During this initial period, cation depletion at the cathode is supposed uniform. Simultaneously, in a very narrow region near the cathode a local charge develops, giving rise to Coulombic forces initially pointing towards the cathode.

After a few seconds, an instability develops, triggering the growth of a deposit at the cathode. The deposit develops as a 3D array of thin porous metallic filaments. Coulombic forces concentrate at the tips according to a model developed in Ref. [9] (cf. also references therein); each porous filament allows fluid to penetrate its tip and to be ejected from the sides, forming a vortex pair in the plane of the growth driven by the electric force. Figure 5 reproduced from [12] shows a top view of the cell with a pair of counter-rotating vortices, as described in Ref. [9].

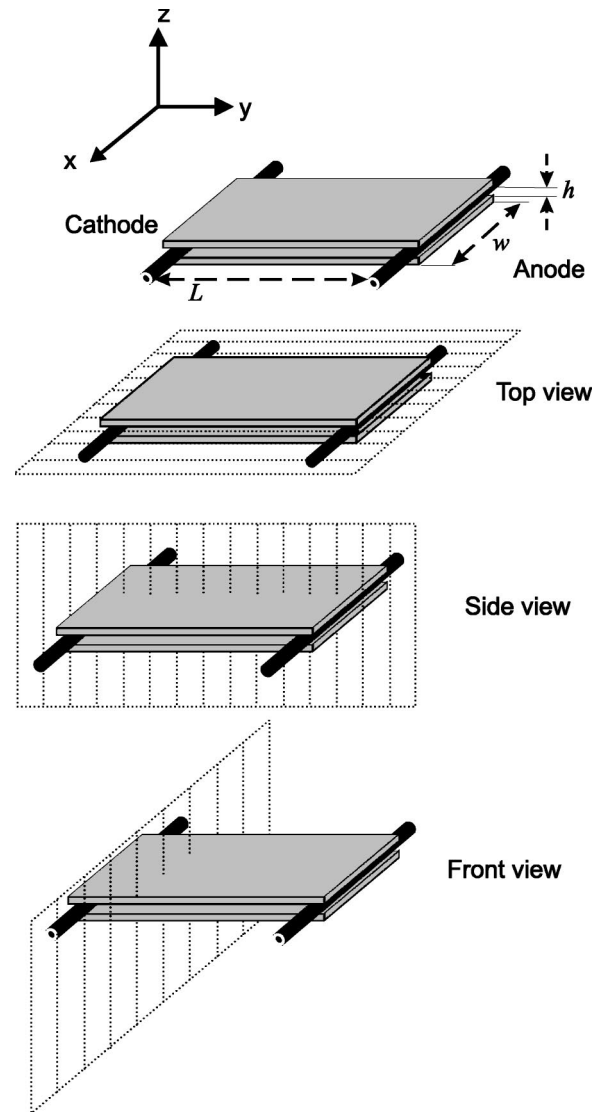


FIG. 3. Experimental setup and cell view convention.

The above-mentioned phenomenological description is based on two-dimensional horizontal and vertical measurements [9,12,19,20]. Although three-dimensional experimental measurements are lacking, pioneering observations of vortex rings were reported in Refs. [9–11], where it was shown that they can form capillary tubes. These observations allowed the heuristic formulation of a 3D model for electroconvection dominated flows in which vortex rings exist in the vicinity of growing deposits and concentration fronts

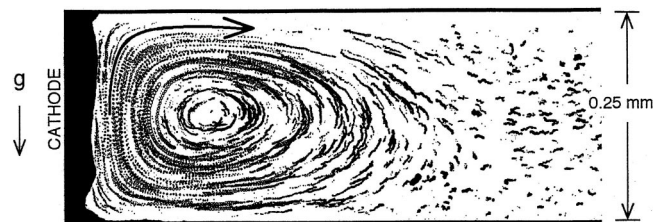


FIG. 4. Side view of the cathodic roll visualized with tracer particles for conditions in which gravity convection is dominant.

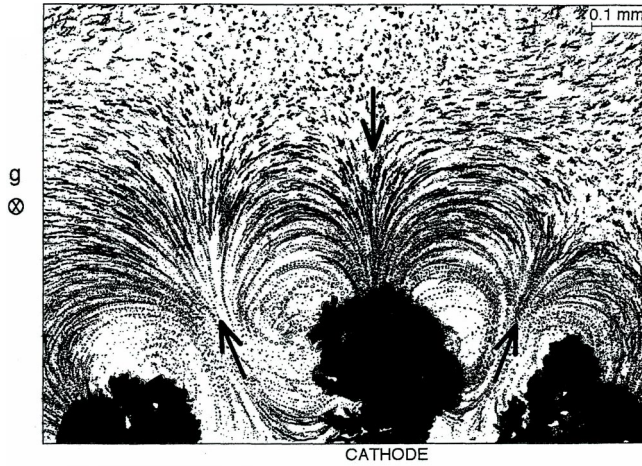


FIG. 5. Top view of the vortex ring visualized with tracer particles for conditions in which electroconvection is dominant.

having the shape of domes were conjectured.

The interaction among vortex pairs due to electric forces, the cathodic concentration front due to chemical reactions, and the cathodic roll due to gravity forces in the presence of ramified deposits, their collision with the anodic roll and concentration front, and the subsequent effect on the deposit morphology is a complex 3D problem. A glimpse of this is provided in Fig. 2 showing a top view of the superposition of electrically driven vortex rings with gravity-driven vortex rolls at dendrite tips. Moreover, the interaction of all transport modes and deposit front yields an entangled 3D helicoidal fluid motion. In fact, to address this problem a generalized 3D phenomenological model is needed. Models to date based on 2D measurements and simulations are by necessity incomplete. Here we present such a generalized model with the help of first principles written as a 3D dimensionless mathematical model and its numerical simulation. As shown below the model introduced reveals the existence of many of the most relevant features of ECD.

II. THEORETICAL ANALYSIS

Ion transport in thin-layer ECD can be described with a mathematical model based on first principles [26–29], including the Nernst-Planck equations for ion transport, the Poisson equation for the electric potential, and the Navier-Stokes equations for the fluid flow (2D models were introduced in Refs. [17,18]). The 3D dimensionless system of equations can be written as

$$\frac{\partial C_i}{\partial t} = -\nabla \cdot \mathbf{j}_i, \quad (1)$$

$$\mathbf{j}_i = -M_i C_i \nabla \phi - \frac{1}{\text{Pe}_i} \nabla C_i + C_i \mathbf{v}, \quad (2)$$

$$\nabla^2 \phi = \text{Po} \sum_i z_i C_i, \quad (3)$$

$$\begin{aligned} \frac{\partial \boldsymbol{\zeta}}{\partial t} + \nabla \times (\boldsymbol{\zeta} \times \mathbf{v}) \\ = \frac{1}{\text{Re}} \nabla^2 \boldsymbol{\zeta} + \sum_i \left[G_{e_i z_i} (\nabla \phi \times \nabla C_i) - G_{g_i} (\nabla C_i) \cdot \frac{\mathbf{g}}{g} \right], \end{aligned} \quad (4)$$

$$\boldsymbol{\zeta} = -\nabla^2 \Psi, \quad (5)$$

$$\mathbf{v} = \nabla \times \Psi. \quad (6)$$

Here C_i and \mathbf{j}_i are the dimensionless concentration and flux of an ionic species i (for a ternary electrolyte such as $\text{ZnSO}_4/\text{H}_2\text{SO}_4$, $i = C, A$, and H , standing for zinc, sulfate, and hydrogen ions, respectively); \mathbf{v} , ϕ , $\boldsymbol{\zeta}$, and Ψ are the dimensionless fluid velocity, electrostatic potential, vorticity vector, and velocity potential vector, respectively; \mathbf{g}/g is a unit vector pointing in the direction of gravity. The quantities $M_i = \mu_i \Phi_0 / x_0 u_0$, $\text{Pe}_i = x_0 u_0 / D_i$, $\text{Po} = x_0^2 C_0 e / \epsilon \Phi_0$, $\text{Re} = x_0 u_0 / \nu$, $G_{e_i} = e C_i \Phi_0 / \rho_0 u_0^2$, and $G_{g_i} = x_0 C_i g \alpha_i / u_0^2$ stand for the dimensionless migration, Peclet, electric Poisson, Reynolds, electric Grashof, and gravity Grashof numbers, respectively. The quantities z_i , μ_i , and D_i are, respectively, the number of charges per ion, mobility, and diffusion constants of an ionic species i ; μ_i and z_i are signed quantities, being positive for cations and negative for anions; g is the dimensional gravitational acceleration; e is the electronic charge, ϵ is the permittivity of the medium, and ν is the kinematic viscosity. x_0 , u_0 , ϕ_0 , C_0 , and ρ_0 are reference values of length, velocity, electrostatic potential, concentration, and fluid density, respectively. For system closure, a Boussinesq-like approximation has been used for the fluid density: $\rho = \rho_0 (1 + \sum_i \alpha_i \Delta C_i)$, where $\alpha_i = (1/\rho_0) \partial \rho / \partial C_i$.

Systems (1)–(6), with appropriate initial and boundary conditions, are valid in a space-time domain defined by $\mathbf{G} = [\boldsymbol{\Omega}(\mathbf{t}) \times (0, \mathbf{t})]$, where $\boldsymbol{\Omega}$ is a three-dimensional region with boundary $\Gamma(t)$; this boundary moves with speed proportional to the norm of the flux \mathbf{j}_i . The boundary conditions for the velocity potential vector are discussed, for instance, in Ref. [30]: in a plane impermeable surface, the vector is normal to the surface and its gradient is 0; at nonslip surfaces, the tangential derivative of the velocity components are 0.

Whether a gravitoconvective or an electroconvective regime prevails, both share the Migration, Peclet, Electric Poisson, Froude, and Reynolds numbers, and differ in the Grashof numbers acting on the Navier-Stokes equations. In the limiting case of a pure electroconvection-driven flow, such as an ECD experiment in a microgravity environment, the electric Grashof number governs the flow; when gravitoconvection prevails, the gravity Grashof number, governs the flow. Increasing the electric or gravity Grashof numbers, increases electro- or gravitoconvection, respectively.

The computational model solves the previous 3D system of equations, for each time step, in a fixed or variable domain, in a 3D uniform lattice, using finite difference and deterministic relaxation techniques. Its solution is obtained via the system of difference equations:

$$\mathbf{W}_k^{n+1} = \sum_j \mathbf{a}_j \mathbf{W}_j^n, \quad (7)$$

where j represents the nearest-neighbor site of the site k ; the summation ranges over all nearest-neighbor sites; \mathbf{W}_k is a vector-valued function whose components are the concentrations C_i , the electrostatic potential ϕ , the vorticity vector ζ and velocity potential vector Ψ ; and \mathbf{a}_j is a diagonal matrix whose elements contain the nonlinear coefficients of the discretized equations. The resulting solution \mathbf{W}_k^{n+1} is then used to advance the interface with a dielectrical breakdown model (DBM) [31]. The interface is moved at random, proportionate to the flux of cations, i.e.,

$$p_k = \frac{|\mathbf{j}_{ck}|}{\sum_i |\mathbf{j}_{ci}|}, \quad (8)$$

where k is a nearest-neighbor site to the interface, p_k is the probability of selecting the nearest-neighbor site k to advance the interface, the summation is over all nearest-neighbor sites i to the interface, and \mathbf{j}_{ck} is the flux of cations flowing from the neighbor site k into the aggregation.

In our simulations the following set of dimensionless numbers remain constant: $M_a = 1$, $M_c = 0.66$, $Pe_a = 12$, $Pe_c = 16$, $Po = 5 \times 10^2$, and $Re = 12 \times 10^{-3}$. Figures are constructed with the excellent graphics software package OPENDX [32].

III. THE LIMITING CASES OF PURE GRAVITY AND PURE ELECTRICALLY DRIVEN CONVECTION

Here we analyze ECD simulations when gravity or electroconvection are absent. Although these cases do not correspond to real problems, they serve to study the separated effects of electric and gravity forces. The first instant of a simulated ECD experiment in which the cathode is shaped with a thin spike, in the limiting case of a gravitoconvective regime ($G_e = 10^{-4}$ and $G_g = 10^4$) is presented in Fig. 6. The cathode with a spike (instead of a flat surface) is chosen in order to compare with simulations of electroconvection dominated flows shown below. Figure 6 shows a top-rear view of the cell with the cathode having a spike. The cathodic and anodic rolls are represented by the isosurface of the modulus of the velocity potential vector (thresholded to eliminate very low velocities). As previously discussed, density current generates gravity-driven rolls consisting in horizontal cylinders squeezed at their extremes due to lateral wall effects (this is evident in the next figure). While the anodic roll remains undisturbed, the cathodic roll is wrapped around the electrode spike. Figure 7 presents the cathodic cell zone (enlarged) showing a top view of an horizontal cross section (at spike level) of the vector velocity field and an anion concentration isosurface (gray area). The figure clearly shows the roll velocity distribution (null at the walls).

Figure 8 displays a geometric form with the approximate shape of a spherical drop (gray area turned slightly transparent) representing an isosurface of the modulus of the electric field, and a top view of an horizontal cross section (at spike

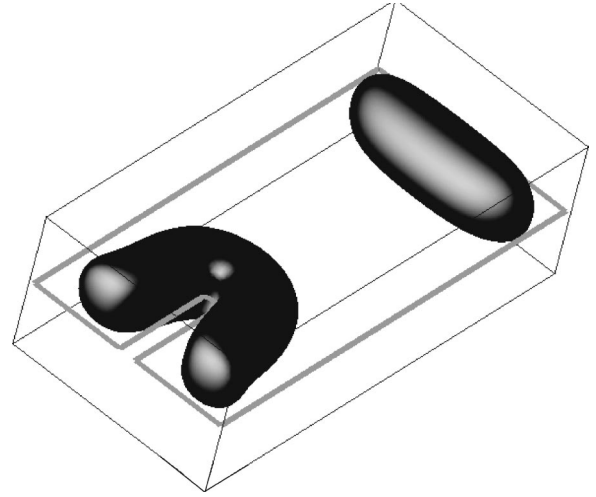


FIG. 6. Top-rear view of rolls represented as an isosurface of the modulus of the velocity potential vector, in the limiting case of a gravitoconvective regime: $G_e = 10^{-4}$ and $G_g = 10^4$ (mesh size $120 \times 60 \times 40$).

level) of the electric field lines. The approximate spherical shape of the drop is due to the value of the modulus of the electric field (thresholded): constant in a large portion of the cell and only increasing its value near the finger tips. The electric field lines converging to the filament tip are clearly seen in the figure. The drop approximately indicates the space zone inside which there is absence of electroneutrality. In fact, the exact computational zone where electroneutrality is absent can be obtained by the surface of the function defined by the difference between the cation and anion concentration ($\sum_i z_i C_i$). This surface is approximately represented by the drop; we have termed it the electric spherical drop.

The first instants of a simulated ECD experiment with a grown deposit, in a microgravity environment ($G_e = 10^4$ and $G_g = 10^{-4}$), is shown in Fig. 9. The figure reveals a dramatic view of the vortex ring crowning the finger tip, represented

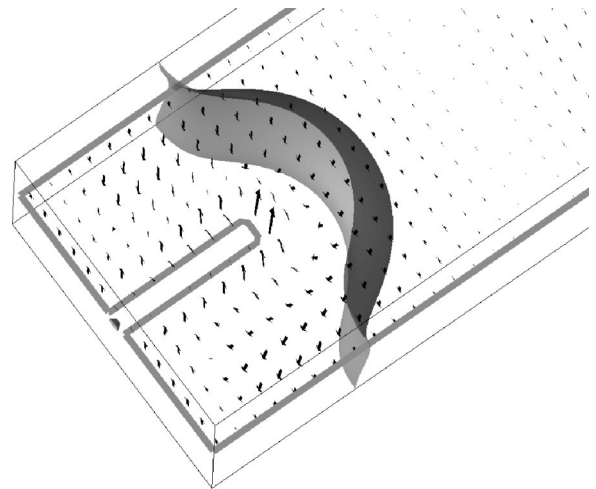


FIG. 7. Cathodic cell zone (enlarged) showing a top view of an horizontal cross section (at spike level) of the vector velocity field and an anion concentration isosurface (gray area), in the limiting case of a gravitoconvective regime: $G_e = 10^{-4}$ and $G_g = 10^4$.

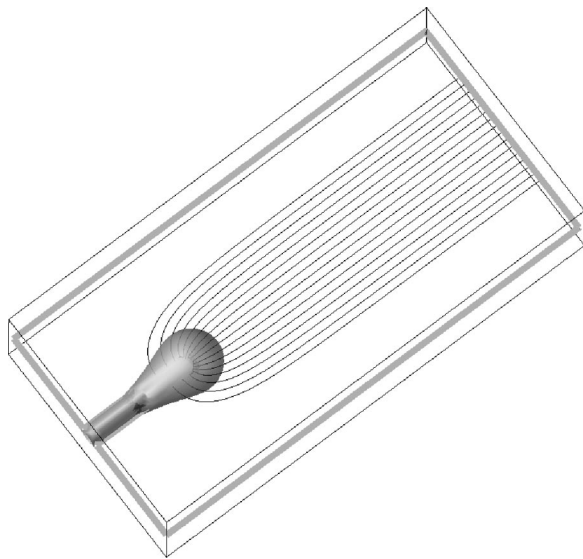


FIG. 8. An isosurface of the modulus of the electric field (gray area) having the approximate shape of a spherical drop (electric spherical drop), and a top view of an horizontal cross section (at spike level) of the electric field lines, in the limiting case of a gravitoconvective regime ($G_e = 10^{-4}$ and $G_g = 10^4$).

as the isosurface of the modulus of the velocity potential vector.

Figure 10 depicts the cathodic cell zone (enlarged) showing a side view of a vertical cross section (at spike level) of the vector velocity field and an anion concentration isosurface (gray area). Concentration isosurfaces surrounds dendrite tips as semispherical shells. This picture shows the characteristic pattern of 2D dipoles crowned by a concentration arc that separates depleted and concentrated solution zones found in the experiments (see, for instance, Fig. 4 from Ref. [7]).

IV. THE MIXED CASE: GRAVITY AND ELECTRICALLY DRIVEN CONVECTION

In the following we analyze ECD simulations in a mixed regime, that is, when gravity and electrically driven convec-

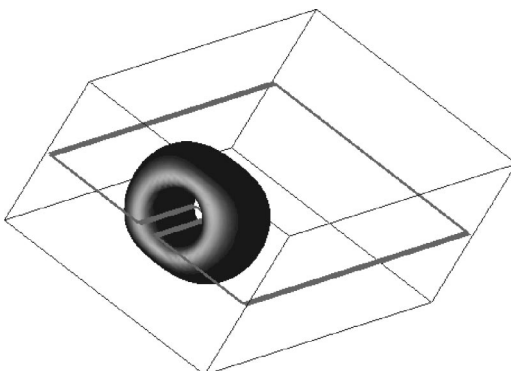


FIG. 9. Top-rear view of a vortex ring represented as the isosurface of the modulus of the velocity potential vector, in the limiting case of an electroconvective regime ($G_e = 10^4$ and $G_g = 10^{-4}$).

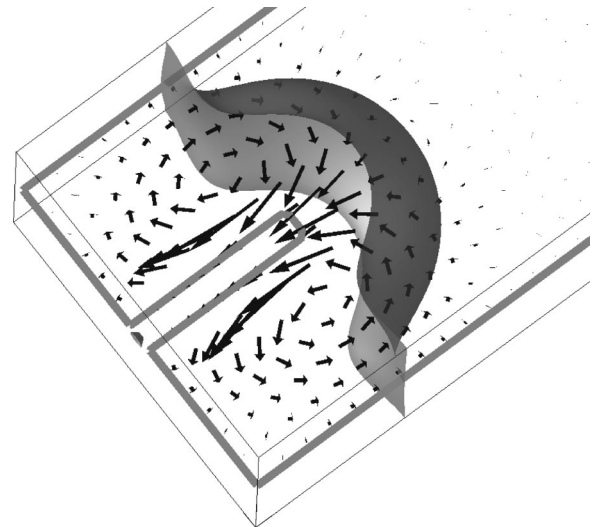


FIG. 10. Cathodic cell zone (enlarged) showing a top view of an horizontal cross section (at spike level) of the vector velocity field and an anion concentration isosurface (gray area), in the limiting case of an electroconvective regime ($G_e = 10^4$ and $G_g = 10^{-4}$).

tions are both relevant in ion transport. Their behavior, typical of real problems, can be more easily explained in terms of the ideal cases previously examined. In the first simulation, gravity-driven convection is dominant over electroconvection, and in the second, the opposite occurs. The aim is to compare with experiments presented in Figs. 4 and 5.

Figures 11 and 12 present the simulation of an ECD experiment under gravitoconvective prevailing conditions ($G_e = 0.5 \times 10^4$ and $G_g = 10^4$). These figures show the rolls and the isosurface of the anion concentration, and superimposed, a vertical cross section of the vector velocity field, respectively. Figure 12 shows again one of the concentration isosurfaces of the spherical shell surrounding the dendrite tip and separating depleted and concentrated solution zones. The velocity distribution in the vertical plane resembles the experimental results of Fig. 4 depicting the gravitoconvective rolls.

Figures 13 and 14 present the simulation of an ECD ex-

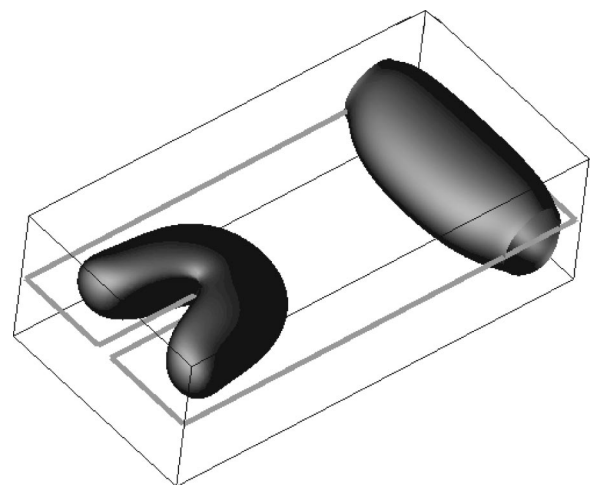


FIG. 11. Top-rear view of rolls under a gravitoconvective predominant regime ($G_e = 0.5 \times 10^4$ and $G_g = 10^4$).

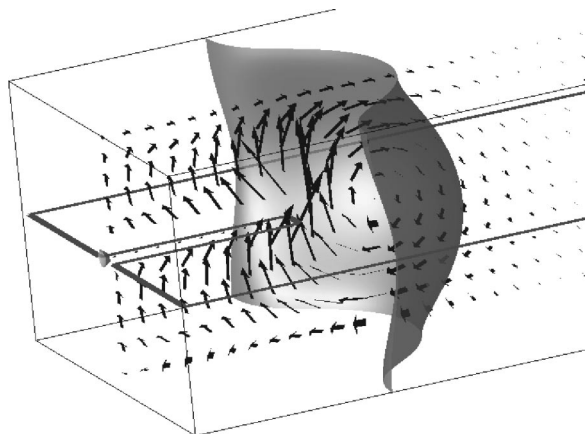


FIG. 12. Cathodic cell zone (enlarged) showing a top view of a horizontal cross section (at spike level) of the vector velocity field and an anion concentration isosurface (gray area with a degree of transparency), in the limiting case of a gravitoconvective regime ($G_e = 0.5 \times 10^4$ and $G_g = 10^4$).

periment under electroconvective prevailing conditions ($G_e = 5 \times 10^4$ and $G_g = 10^4$). Figure 13 reveals the cathodic roll, superimposed to the vortex ring, interacting between themselves and wrapping the dendrite tip. Compare Fig. 13 with Fig. 9 to see the effect of gravitoconvection over the vortex ring: a suppression of the lower zone of the vortex ring and an enhancement of the lateral zones (next figure shows the vector composition in more detail). In Fig. 14, roll and vortex rings coincide in space with the concentration shell, generating a surface with a dome shape. The concentration shell and the cathodic roll and the vortex ring separate the depleted and concentrated solution zones. The velocity distribution in the horizontal plane resembles the experimental results of Fig. 5 depicting the 2D counter rotating vortices.

V. VORTEX COALESCENCE, COLLISION AND MERGING

The aim of this section is to present vortex interaction among themselves in the presence of several dendrites, in an

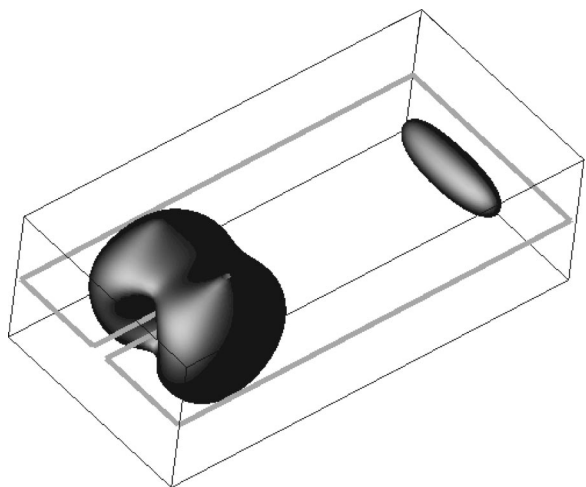


FIG. 13. Anodic roll (undisturbed) and cathodic roll merged with the vortex ring under electroconvective prevailing conditions ($G_e = 5 \times 10^4$ and $G_g = 10^4$).

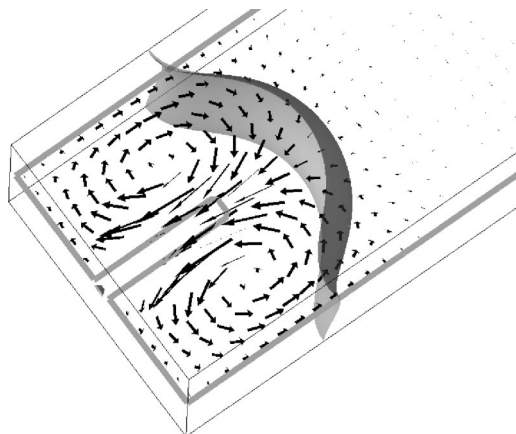


FIG. 14. Enlarged plot of the cathodic cell zone showing a top view of an horizontal cross section (at spike level) of the vector velocity field and an anion concentration isosurface (gray area), under electroconvective prevailing conditions for $G_e = 5 \times 10^4$ and $G_g = 10^4$.

analogy with the physical experiment of Fig. 2. Figures 15–18 present simulated ECD experiments, under gravitoconvective prevailing conditions for $G_e = 10^4$ and $G_g = 2 \times 10^4$, when five fingers are grown at a different speed. These figures show the precise moment in which the cathodic and anodic rolls collide and merging starts. There is a coalescence among individual rolls of adjacent filament tips, resulting in a more uniform cathodic front. This front is defined by dendrites and their vortex rings pushing the front forward. These simulations have some resemblance with the lower five fingers of Fig. 2.

Figure 17 shows trajectories of particles released near the dendrite tips. They reveal the entangled nature of flow: near the dendrite tips the fluid is entrained by vortex rings whose basin of attraction is the dendrite tip. However, some particles manage to escape and are entrained by the vortex roll, finally orbiting with an helicoidal motion. Figure 18 reveals the coalescence of the individual electric spherical drops. This phenomenon has a definite influence on dendrite growth pattern formation as discussed later.

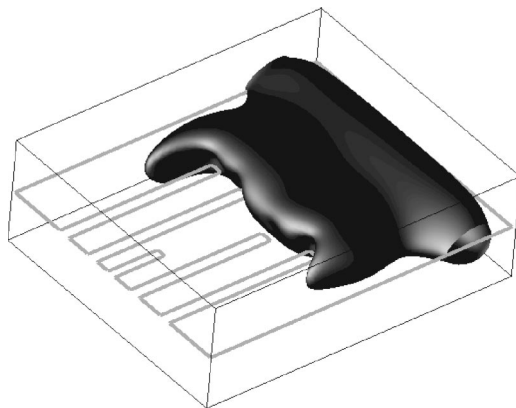


FIG. 15. Five fingers (light gray) and vortices (darker zone) merging under gravitoconvective prevailing conditions: $G_e = 10^4$ and $G_g = 2 \times 10^4$ (mesh size $100 \times 120 \times 40$).

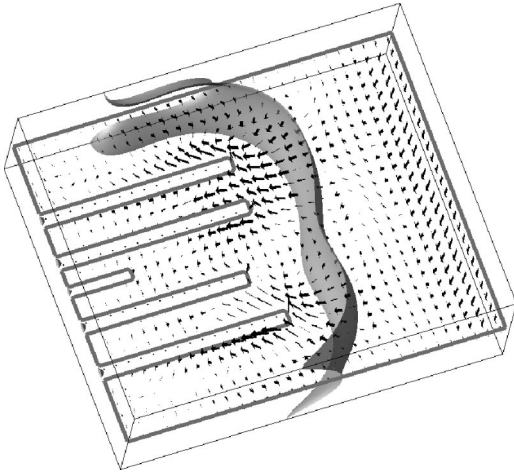


FIG. 16. Enlarged plot of the cathodic zone showing a top view of an horizontal cross section (at finger level) of the vector velocity field and an anion concentration isosurface (gray area), under gravitoconvective prevailing conditions for $G_e = 10^4$ and $G_g = 2 \times 10^4$.

VI. DISCUSSION

When dendrites grow through an electrochemical thin-layer cell, they encounter complex 3D ion transport phenomena. Here we introduced a generalized 3D macroscopic model that allows full ion transport mode interaction in the presence of dendrites, in particular, when convection prevails. In this case, electroconvection and gravitoconvection are governed by the electric and gravity Grashof numbers, respectively. In the limiting case of a gravitoconvective dominant flow, the model predicts the existence of concentration shells and convection rolls near each electrode expanding toward one another, and the interaction mode with ramified deposits: the shell and roll bend and surround filaments forming a sort of three-dimensional envelope tube squeezed by the filament tip and slaved to the deposit front. In the limiting case of a microgravity experiment, the model predicts the existence of vortex rings and electric spherical drops due to electric forces on space charges accumulating

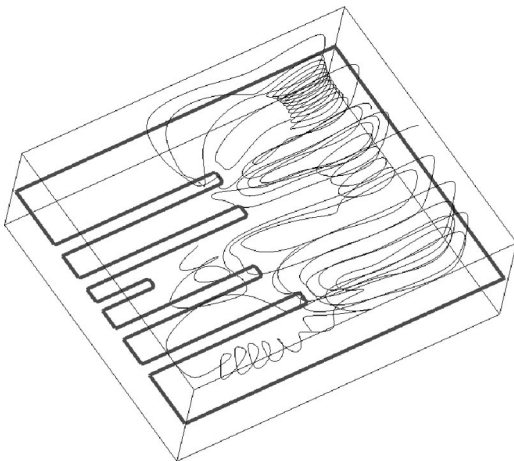


FIG. 17. Particle trajectories (released near the dendrite tips) under gravitoconvective prevailing conditions for $G_e = 10^4$ and $G_g = 2 \times 10^4$.

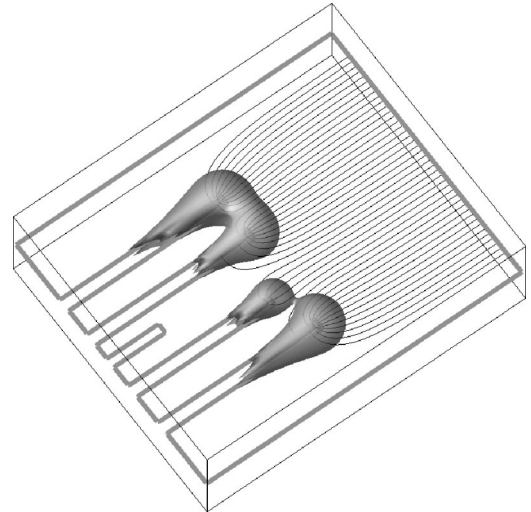


FIG. 18. Electric spherical drops (gray area) representing an isosurface of the modulus of the electric field and a top view of an horizontal cross section (at spike level) of the electric field lines, under gravitoconvective prevailing conditions for $G_e = 10^4$ and $G_g = 2 \times 10^4$.

near the growing filament tip. When both numbers are relevant, ion transport near the growing dendrite tips is the result of the combined action of vortex rings, electric spherical drops, concentration shells and rolls. Simulations reveal that as Grashof numbers vary, all the variables have substantial variations except the electric field that can be shown to remain fairly constant.

Although the simulation of limiting cases do not model real experiments, they are interesting in their own because they reveal the characteristic features of each individual force action. The simulation of mixed cases unveils the complex pattern present in experiments and is better understood through the analysis of limiting cases. The transition from gravitoconvection to electroconvection prevailing conditions can be analyzed with the ratio $\lambda = G_g / G_e$ [18]. The value of λ for the experiment of Fig. 4 is twice that of the experiment of Fig. 5, consistent with the observation of greater relative influence of gravitoconvection in the experiment of Fig. 4. The experimental transition presented in these figures was obtained varying cell thickness and current density. To simulate such a transition, the value of λ in Fig. 12 was chosen one order of magnitude larger than that of Fig. 14. Simulations reveal that the roll of Fig. 12 resembles the experimental roll of Fig. 4, and the vortex ring (horizontal cross section) of Fig. 14, the experimental one of Fig. 5. Due to numerical stability constrains, the electric Poisson and Grashof numbers used in the simulated transition are several orders of magnitude smaller than typical experimental values [20], thus introducing artificial damping. They can be thought as simulating an experiment with a smaller elementary charge. Nevertheless, simulated and experimental results are remarkably close.

Simulations help in the elucidation of sustained dendritic growth and dendritic selection. Fig. 18, simulating a gravitoconvective prevailing regime as that of Fig. 2, shows the foremost dendrites concentrating the electric field lines (thus,

the migratory cation flux) and, because of the existence of the electric vortex rings (present in this regime), also most of the convective cation flux. Thus, the foremost dendrites concentrate the incoming cation flux in a sort of funneling; in this way dendrite growth is sustained. When, due to random flux disturbances, one tip is retarded in its growth relative to its neighbors, quickly gets out of the incoming material flux and stops growing, as can be observed in Fig. 2. This is reflected in the simulations of Figs. 16 and 18.

Further, our model makes it possible to prove numerically from first principles the existence of 3D structures, and therefore it leads to a more complete formulation of a 3D phenomenological model and its space-time evolution: rolls are vortex tubes squeezed at their ends, concentration fronts

form shells accompanying rolls, electric spherical drops are isosurfaces of the modulus of the electric field, rolls and shells envelope filaments, among other features. Thus, the model not only correctly predicts 2D experimental measurements found in the literature but also provides insights into the physical problem. The experiments and modeling of the complex ECD ion convective transport behavior can be governed by just two numbers: the gravity and electric Grashof numbers.

ACKNOWLEDGMENTS

This work was partially supported by UBA Grant No. TX09/99 and CONICET Grant No. PIP379/98.

-
- [1] T. Vicsek, *Fractal Growth Phenomena*, 2nd ed. (World Scientific, Singapore, 1992).
- [2] F. Argoul, J. Huth, P. Merzeau, A. Arneodo, and H.L. Swinney, *Physica D* **62**, 170 (1993).
- [3] R.M. Brady and Ball, *Nature (London)* **309**, 225 (1984).
- [4] V. Fleury, J.N. Chazalviel, M. Rosso, and B. Sapoval, *Phys. Rev. A* **44**, 6693 (1991).
- [5] V. Fleury, J.N. Chazalviel, and M. Rosso, *Phys. Rev. Lett.* **68**, 2492 (1992).
- [6] V. Fleury, J.N. Chazalviel, and M. Rosso, *Phys. Rev. E* **48**, 1279 (1993).
- [7] V. Fleury, J. Kaufman, and B. Hibbert, *Nature (London)* **367**, 435 (1994).
- [8] K.A. Linehan and J.R. de Bruyn, *Can. J. Phys.* **73**, 177 (1995).
- [9] V. Fleury, M. Rosso, and J.N. Chazalviel, in *Fractal Aspects of Materials*, edited by F. Family, B. Sapoval, P. Meakin, and R. Wool, Mater. Res. Soc. Symp. Proc. 367 (Material Research Society, Pittsburgh, 1995), p. 183.
- [10] V. Fleury, M. Rosso, and J.-N. Chazalviel, in *Defect Structure, Morphology and Properties of Deposits*, edited by H.D. Merchant (The Mineral, Metals and Materials Society, Warrendale, PA, 1995), p. 195.
- [11] V. Fleury and J.-N. Chazalviel, in *Fractal Aspect of Materials* (Ref. [9]), p. 169.
- [12] J. Huth, H. Swinney, W. McCormick, A. Kuhn, and F. Argoul, *Phys. Rev. E* **51**, 3444 (1995).
- [13] D. Barkey, D. Watt, Z. Liu, and S. Raber, *J. Electrochem. Soc.* **141**, 1206 (1994).
- [14] C. Leger, J. Elezgaray, and F. Argoul, *Phys. Rev. Lett.* **78**, 5010 (1997).
- [15] J.N. Chazalviel, *Phys. Rev. A* **42**, 7355 (1990).
- [16] G. Marshall, E. Perone, P. Tarela, and P. Mocskos, *Chaos, Solitons Fractals* **6**, 315 (1995).
- [17] G. Marshall and P. Mocskos, *Phys. Rev. E* **55**, 549 (1997).
- [18] G. Marshall, P. Mocskos, H.L. Swinney, and J.M. Huth, *Phys. Rev. E* **59**, 2157 (1999).
- [19] S. Dengra, G. Marshall, and F. Molina, *J. Phys. Soc. Jpn.* **69**, 963 (2000).
- [20] G. Gonzalez, G. Marshall, F.V. Molina, S. Dengra, and M. Rosso, *J. Electrochem. Soc.* **148**, C479 (2001).
- [21] G. Gonzalez, G. Marshall, F.V. Molina, and S. Dengra *Phys. Rev. E* **65**, 051607 (2002).
- [22] J.C. Bradley, H.M. Chen, J. Crawford, J. Eckert, K. Ernazarova, T. Kurzeja, M. Lin, M. McGee, W. Nadler, and S.M. Stephens, *Nature (London)* **389**, 268 (1997).
- [23] J.C. Bradley, S. Dengra, G.A. Gonzalez, G. Marshall, and F.V. Molina, *J. Electroanal. Chem.* **478**, 128 (1999).
- [24] K.D. Hermanson, S.O. Lumsdon, J.P. Williams, E.W. Kaler, and O.D. Velev, *Science* **294**, 1082 (2001).
- [25] Y. Fukunaka, K. Okano, Y. Tomii, and Z. Asaki, *J. Electrochem. Soc.* **145**, 1876 (1998).
- [26] A.J. Bard and L.R. Faulkner, *Electrochemical Methods, Fundamentals and Applications* (Wiley, New York, 1980).
- [27] J.S. Newman, *Electrochemical Systems* (Prentice Hall, Englewood Cliffs, NJ, 1973).
- [28] Ronald F. Probstein, *Physicochemical Hydrodynamics, An Introduction* (Wiley, New York, 1994).
- [29] V.G. Levich, *Physicochemical Hydrodynamics* (Prentice Hall, Englewood Cliffs, NJ, 1962).
- [30] G.D. Mallinson and G. de Vahl Davis, *J. Comput. Phys.* **12**, 435 (1973).
- [31] L. Pietronero and H.J. Weismann, *J. Stat. Phys.* **36**, 909 (1984).
- [32] The latest version of OPENDX for Linux is available over the World Wide Web at <http://www.opendx.org>.